



HAL
open science

Nonlinear Wave–Wave Coupling Related to Whistler-mode and Electron Bernstein Waves Observed by the Parker Solar Probe

Jiuqi Ma, Xinliang Gao, Zhongwei Yang, Bruce Tsurutani, Mingzhe Liu, Quanming Lu, Shui Wang

► To cite this version:

Jiuqi Ma, Xinliang Gao, Zhongwei Yang, Bruce Tsurutani, Mingzhe Liu, et al.. Nonlinear Wave–Wave Coupling Related to Whistler-mode and Electron Bernstein Waves Observed by the Parker Solar Probe. The Astrophysical Journal, 2021, 918 (1), pp.26. <10.3847/1538-4357/ac0ef4>. <hal-03660812>

HAL Id: hal-03660812

<https://hal.science/hal-03660812v1>

Submitted on 1 Aug 2025

HAL is a multi-disciplinary open access archive for the deposit and dissemination of scientific research documents, whether they are published or not. The documents may come from teaching and research institutions in France or abroad, or from public or private research centers.






L'archive ouverte pluridisciplinaire **HAL**, est destinée au dépôt et à la diffusion de documents scientifiques de niveau recherche, publiés ou non, émanant des établissements d'enseignement et de recherche français ou étrangers, des laboratoires publics ou privés.



Distributed under a Creative Commons CC BY 4.0 - Attribution - International License



Nonlinear Wave–Wave Coupling Related to Whistler-mode and Electron Bernstein Waves Observed by the Parker Solar Probe

Jiuqi Ma^{1,2} , Xinliang Gao^{1,2} , Zhongwei Yang^{1,2,3} , Bruce T. Tsurutani⁴, Mingzhe Liu⁵ , Quanming Lu^{1,2} , and Shui Wang^{1,2}

¹ CAS Key Laboratory of Geospace Environment, Department of Geophysics and Planetary Science, University of Science and Technology of China, Hefei, People's Republic of China; gaoxl@mail.ustc.edu.cn

² CAS Center for Excellence in Comparative Planetology, Hefei, People's Republic of China

³ State Key Laboratory of Space Weather, National Space Science Center, Chinese Academy of Sciences, Beijing, People's Republic of China

⁴ Retired, Pasadena, CA, USA

⁵ LESIA, Paris Observatory, PSL University, CNRS, Sorbonne University, University of Paris 5, Place Jules Janssen, F-92195 Meudon, France

Received 2021 June 7; revised 2021 June 17; accepted 2021 June 25; published 2021 September 1

Abstract

We report nonlinear wave–wave coupling related to whistler-mode or electron Bernstein waves in the near-Sun slow solar wind with Parker Solar Probe (PSP) data. Prominent plasma wave power enhancements usually exist near the electron gyrofrequency (f_{ce}), identified as electrostatic whistler-mode and electron Bernstein waves (Malaspina et al. 2020). We find that these plasma waves near f_{ce} typically have a harmonic spectral structure and further classify them into three types identified by the characteristics of wave frequency and electric power. For short, we will call these type I, type II, and type III waves. The first (type I) is the quasi-electrostatic whistler-mode wave and its second harmonic, which resembles the quasi-electrostatic multiband chorus in the Earth's magnetosphere. The second (type II) is the pure electron Bernstein wave. The last (type III) is an intermixture of whistler-mode and electron Bernstein waves, where the wave mode driven by the coupling between them was also detected. During the first five orbits of PSP, the type III spectra have the largest occurrence rate, then the type I spectra. The type II spectra are the rarest type of wave. Our study reveals that nonlinear wave–wave coupling in the solar wind may be as common as in the Earth's magnetosphere.

Unified Astronomy Thesaurus concepts: [Solar wind \(1534\)](#)

1. Introduction

Whistler-mode waves and electron Bernstein waves are prevalent plasma waves in space, such as in the solar wind and in the Earth's magnetosphere (Helliwell 1967; Kennel et al. 1970; Horne et al. 1981; Zhang et al. 1998; Meredith et al. 2009; Wilson et al. 2010). Whistler-mode waves are right-hand polarized electromagnetic emissions falling within the frequency range of lower hybrid frequency to electron cyclotron frequency (f_{ce}) and they were some of the first observed in situ waves in the Earth's magnetosphere (Tsurutani & Smith 1974; Burtis & Helliwell 1969; Thorne 2010). Many previous observations have confirmed the existence of whistler-mode waves in the solar wind from ~ 0.3 to ~ 1 au, and they are typically quasi-parallel, narrowbanded, and have frequencies below $0.5f_{ce}$ (Lacombe et al. 2014; Stansby et al. 2016; Jagarlamudi et al. 2020). During the first two perihelion passes of the Parker Solar Probe (PSP), whistler-mode waves were observed during low-turbulence solar wind intervals. These waves have turned out to be quasi-electrostatic and have very high frequencies near f_{ce} (Malaspina et al. 2020). Whistler-mode waves are a promising candidate for the formation of the halo and strahl populations of electrons in the solar wind (Vocks et al. 2005; Vocks 2012; Kajdič et al. 2016; Tong et al. 2019; Agapitov et al. 2020; Cattell et al. 2021). Electron Bernstein waves, also known as electron cyclotron harmonic (ECH) waves, are electrostatic emissions observed between the harmonics of the electron cyclotron frequency. Electron Bernstein waves have been detected more commonly in Earth's magnetosphere than in the solar wind (Kennel et al. 1970; Fredricks & Scarf 1973). Recently, Malaspina et al. (2020) found electron Bernstein waves in the near-Sun solar wind

using the PSP and suggested they may play a role in regulating the solar heat flux carried by electrons.

The nonlinear wave–wave coupling related to whistler-mode or electron Bernstein waves is very common in the Earth's magnetosphere (Ellis & Porkolab 1968; Harker & Crawford 1968; Gao et al. 2017). Instruments on board the THEMIS satellite detected whistler-mode waves with a second or even a third harmonic (i.e., multiband chorus); these originate from coupling between the electrostatic and magnetic components (or the electrostatic component itself; Gao et al. 2016, 2017). Observations also revealed that one whistler-mode wave can be coupled with one electron Bernstein wave or another whistler-mode wave (Gao et al. 2018b). However, such nonlinear wave–wave coupling related to whistler-mode or electron Bernstein waves has been never reported in the solar wind.

In this study, we report wave–wave coupling related to whistler-mode and electron Bernstein waves in the near-Sun solar wind recorded by PSP up to the present time (with further incursions of PSP to the closeness to the Sun, one expects new and heretofore unknown wave–wave interactions). We find that plasma waves near f_{ce} are always observed along with harmonic spectra, which can be further classified into three types. The first is the quasi-electrostatic whistler-mode wave and its second harmonic. This resembles the quasi-electrostatic multiband chorus in Earth's magnetosphere (Gao et al. 2016). The second is pure electron Bernstein waves. The third is the intermixture of whistler-mode and electron Bernstein waves, where the wave mode driven by the coupling between them is also detected. A full understanding of the nonlinear evolution of these waves may have potential importance to the electron dynamics of the solar wind.

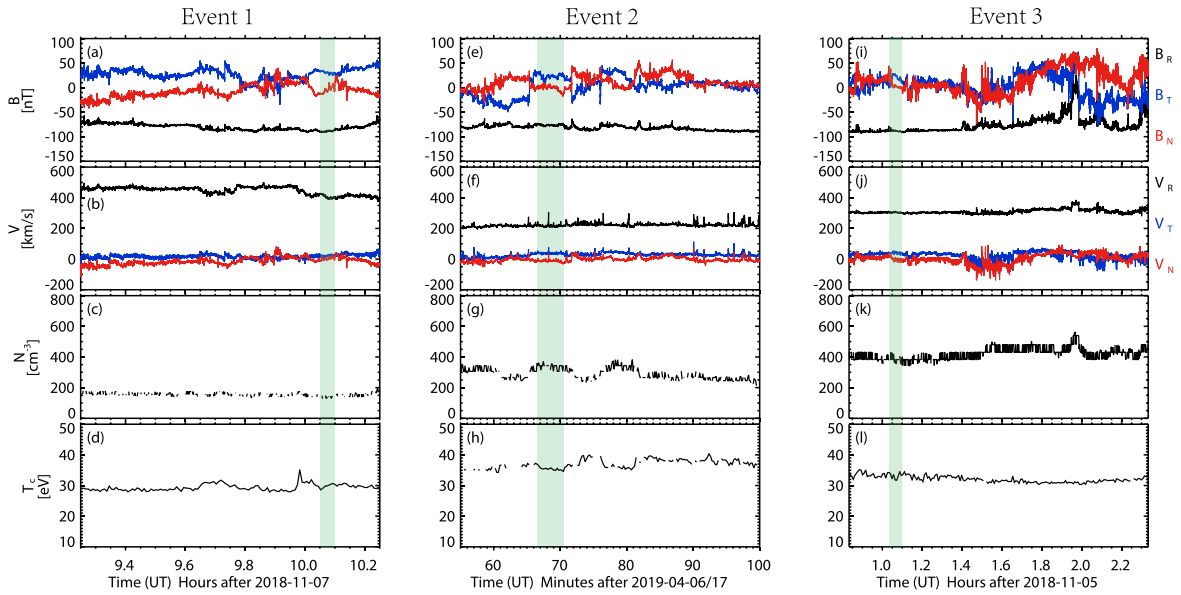


Figure 1. Solar wind conditions for three events. (a) The ambient magnetic field vector in RTN coordinates, (b) proton velocity in RTN coordinates, (c) electron density, and (d) electron core temperature for Event 1. (e)–(h) for Event 2. (i)–(l) for Event 3. The green shaded region marks the time interval when plasma waves are observed.

2. Instruments and Data

Launched in 2018 August, PSP is a mission designed to explore the near-Sun plasma environment, eventually reaching as close as 9.86 solar radii (R_S) from the center of the Sun (Fox et al. 2016). The FIELDS (Bale et al. 2016) equipment suite on board PSP provides in situ measurements of the wave magnetic and electric fluctuations. The plasma data are obtained from the Solar Wind Electrons Alphas and Protons (SWEAP; Kasper et al. 2016) instrument suites. We used the PSP data during the first five orbits and the perihelion distance between $27.8 R_S$ and $35.6 R_S$.

The AC power spectra are calculated for four different channels (electric and magnetic field channels), which are obtained from the FIELDS Digital Fields Board (Malaspina et al. 2016). In this paper we primarily utilized the AC power spectra of differential voltage V_{12} ($= V_1 - V_2$), which covers the frequency range of ~ 140 Hz to 75 kHz and has a high cadence of ~ 0.87 s. The AC power spectra data are organized in 56 pseudo-logarithmically spaced frequency bins. The magnetic field data in RTN (radial-tangential-normal) coordinates at $4.58 \text{ Samples s}^{-1}$ are used for the ambient magnetic field, provided by the Fluxgate Magnetometer (MAG) instrument of the FIELDS suite.

The proton distribution moments are provided by the sunward-facing Solar Probe Cup (SPC) Faraday cup instrument (Case et al. 2020). The bulk velocity of protons is used to indicate the solar wind velocity. The temperature of core electrons is estimated by fitting the electron velocity distribution, which is measured by the Solar Probe Analyzers Electrons (SPAN-E; Whittlesey et al. 2020) with a time resolution of ~ 28 s. Following the method used by Moncuquet et al. (2020), the electron density is calculated from the Quasi-thermal Noise (QTN) spectrum.

3. Observations

Figure 1 presents the solar wind conditions for three time intervals, including the ambient magnetic field (first row), solar

wind velocity (second row), electron density (third row), and electron core temperature (bottom row). The periods that we are interested in, during which the harmonic spectra around the f_{ce} are detected, have been shaded in light green. The location of Event 3 is closest to the Sun, i.e., $\sim 36.6 R_S$, and Events 1 and 2 are observed at ~ 36.9 and ~ 38.2 solar radii (R_S), respectively. All three events are captured during low-turbulence periods with the near-radial ambient magnetic fields (Figures 1(a), (e), and (i)). The ambient solar wind magnetic field is disturbed before and after the wave intervals (shaded regions), but is significantly less disturbed during the wave intervals. This is consistent with the statistical result in Malaspina et al. (2020), where they suggested that the near-radial solar wind magnetic field with weak magnetic field turbulence may be a potential condition for the presence of these near- f_{ce} waves. The three events all occur in slow solar winds, i.e., the solar wind velocity is less than 450 km s^{-1} (Figures 1(b), (f), and (j)). The background plasma density is usually very high (Figures 1(c), (g), and (k)), and the ratios of the plasma frequency to electron gyrofrequency for three events are estimated as ~ 41 , ~ 73 , and ~ 69 , respectively. Thus the plasma beta is quite low, $\beta \leq 0.075$ for the three events.

Using the wave frequency and spectral characteristics, we have found three types of electric spectra along with the harmonic structure around f_{ce} . The above three events are representative examples of the three types of harmonic spectra. The type I spectrum is displayed in Figure 2, which is observed during the time interval shaded in Figure 1(a). Figure 2(a) shows the spectrogram of differential voltage V_{12} from 10:03:45 to 10:06:30 UT, in which the white lines represent f_{ce} , $2f_{ce}$, and $3f_{ce}$, respectively. Two separated frequency bands exit in the spectrogram: one with a larger power, i.e., band 1, is located below f_{ce} (~ 1831 Hz); the other is above f_{ce} (~ 3662 Hz) and has a much lower power, i.e., band 2.

We present the electric power as a function of frequency at 10:03:58 UT in Figure 2(b), when band 1 has maximum wave power ($5.7 \times 10^{-9} \text{ V}^2/\text{Hz}$). In Figure 2(b), the peak frequency f_0 with a dominant power for band 1 has been marked by the

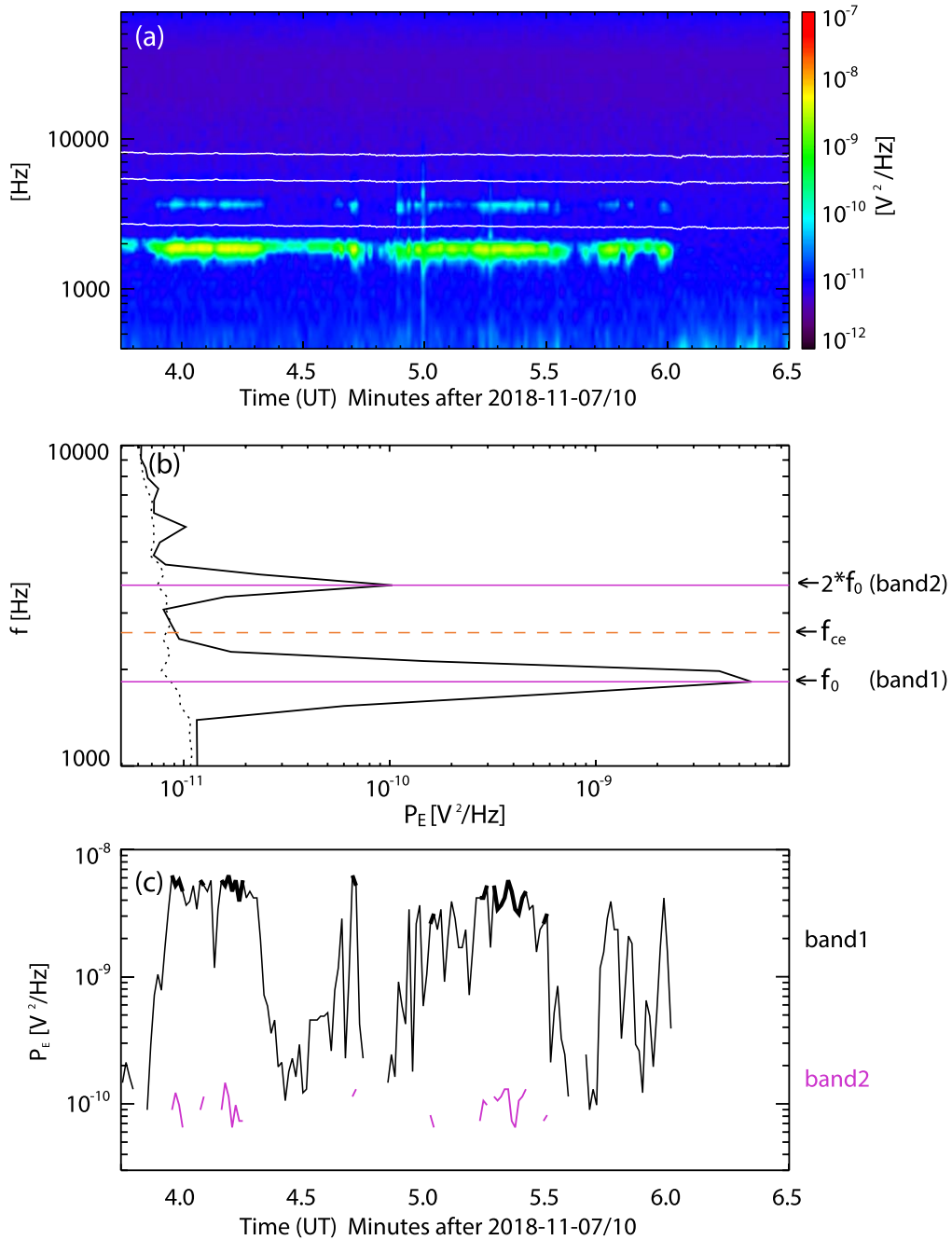


Figure 2. The type I spectrum. (a) Spectrograms of the differential voltage V_{12} , (b) power spectral density P_E vs. the frequency at 10:03:58 UT, and (c) peak power spectral densities P_E for the whistler-mode wave (black) and its second harmonic (magenta). In panel a, solid white lines indicate the electron gyrofrequency f_{ce} and its harmonics. In panel b, the yellow dashed line marks the f_{ce} , and solid magenta lines represent the peak frequencies for two bands. The dotted black line denotes the background noise.

solid magenta line, along with its second harmonic $2f_0$, which coincides with the peak frequency of band 2 very well. We have also plotted the electric power around 10:06:20UT (without wave signal) as the background noise (dotted black line). Here we require that a valid wave signal have an electric power larger than the noise level.

Figure 2(c) shows the time profile of the peak wave power of valid wave signals for two bands. The thicker solid line (band 1) corresponds to the existence of band 2 (solid magenta line), suggesting that the second harmonic is excited only if the amplitude of the fundamental wave (band 1) reaches some threshold. It is found that the electric power of band 1 is

typically 1–2 orders of magnitude larger than band 2. It is worth noting that there is no detectable wave signal near f_{ce} in the magnetic spectrogram during the same interval. For the type I event, we propose that band 1 is a quasi-electrostatic whistler-mode wave, and band 2 is the second harmonic driven by the nonlinear coupling of electrostatic components of band 1. This scenario is quite similar to the quasi-electrostatic multiband chorus in Earth’s magnetosphere (Gao et al. 2018a).

Figure 3 presents the type II spectra near f_{ce} , corresponding to the shaded time interval in Figure 1(e). The format of Figure 3 is the same as in Figure 2. In Figure 3(a), we find that there are four separated frequency bands lying on the electron

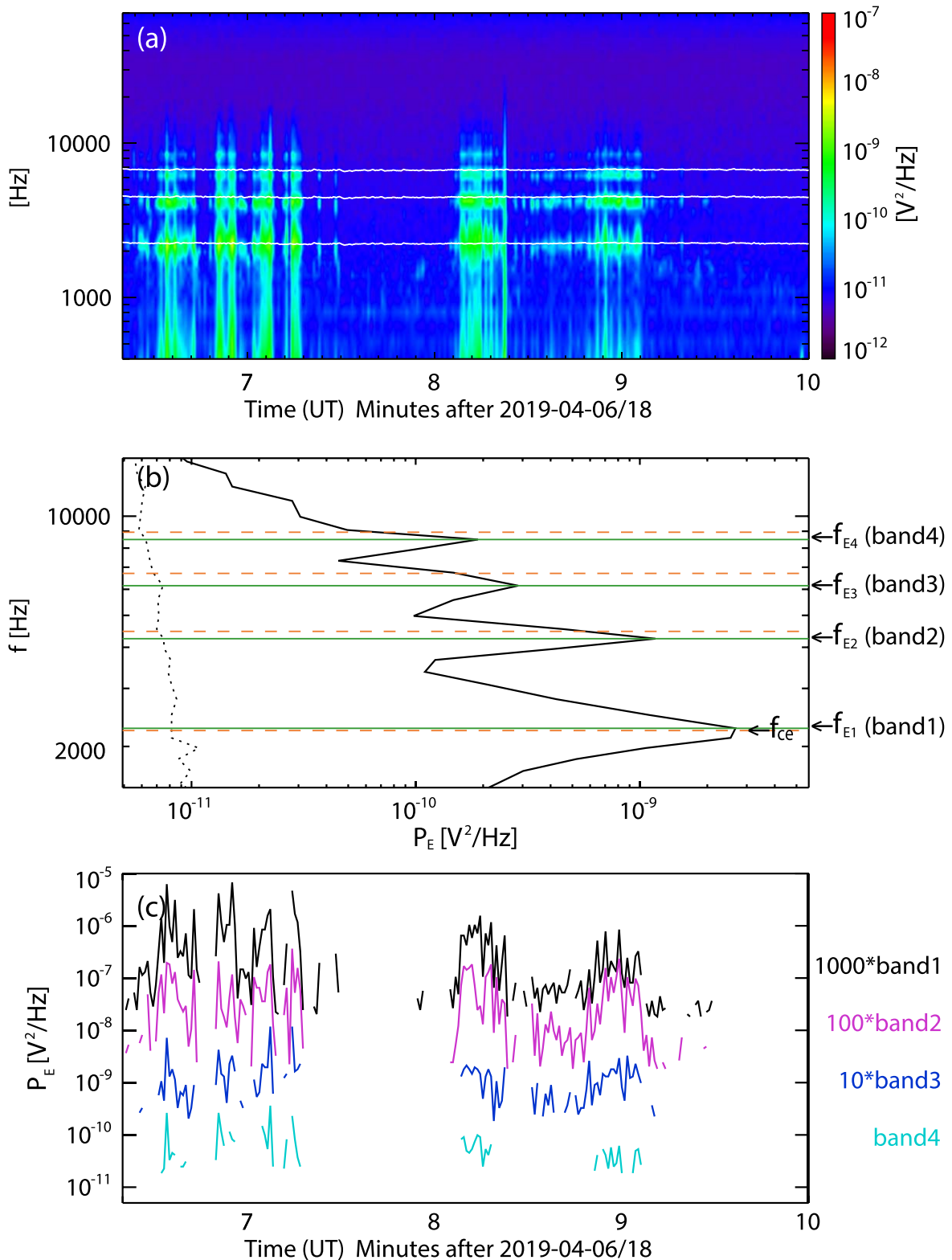


Figure 3. The type III spectrum. (a) Same as Figure 2(a), (b) power spectral density P_E vs. the frequency at 18:06:51 UT, and (c) peak power spectral densities P_E for the first to fourth ECH wave bands (black, magenta, blue, and cyan). In panel a, solid white lines indicate the electron gyrofrequency f_{ce} and its harmonics. In panel b, the dashed yellow lines mark the electron gyrofrequency f_{ce} and its harmonics and the solid green lines represent the peak frequencies for four bands. The dotted black line denotes the background noise. In panel c, peak power spectral densities P_E for the first to third wave bands are multiplied by 1000, 100, and 10.

gyrofrequency and its second, third, and even fourth harmonics. This is further exhibited in Figure 3(b). The electric power as a function of frequency at 18:06:51 UT is shown in Figure 3(b), where we have also marked the harmonics of the

electron gyrofrequency (yellow dashed lines) and peak frequencies (f_{E1} , f_{E2} , f_{E3} , and f_{E4}) for the four bands (solid green lines). It is noted that the power peaks for the four bands are quite close to the first four harmonics of the electron

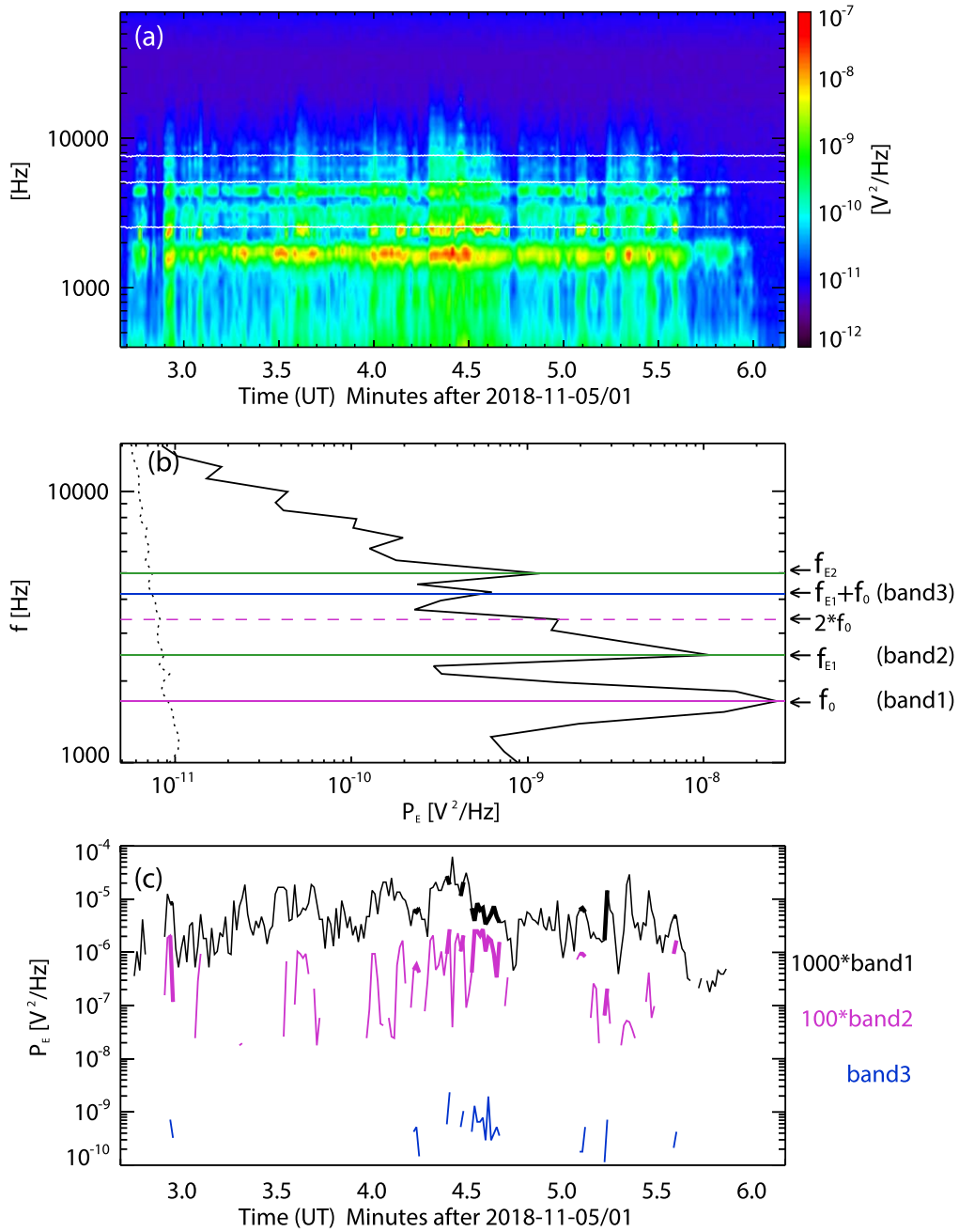


Figure 4. The type III spectrum. (a) Same as Figure 2(a), (b) power spectral density P_E vs. the frequency at 01:04:28 UT, and (c) peak power spectral densities P_E for the whistler-mode wave (black), ECH wave (magenta), and the coupling between the whistler-mode wave and the ECH wave (blue). In panel a, solid white lines indicate the electron gyrofrequency f_{ce} and its harmonics. In panel b, the magenta lines represent the peak frequencies for whistler-mode wave (solid) and its second harmonic (dash), the solid green lines represent the peak frequencies for the first two ECH wave bands, and the solid blue line represents the coupling between the whistler-mode wave and the ECH wave. The dotted black line denotes the background noise. In panel c, peak power spectral densities P_E for band 1 and band 2 are multiplied by 1000 and 100.

gyrofrequency. Second, the power ratio between two adjacent frequency bands is usually less than one order of magnitude, which is also revealed in Figure 3(c), where the time profiles of the peak wave power of valid wave signals for all bands are presented. Again, we require that the electric power is at least one order of magnitude larger than the noise level (dotted black line) for a “valid” signal. The above observed properties of our type II events are consistent with electron Bernstein waves. However, so far, we cannot tell whether the nonlinear wave-wave coupling is involved in type II event generation solely based on the electric spectrogram.

The type III spectrum near f_{ce} is shown in Figure 4, and this event occurs during the shaded time interval in Figure 1(i). In Figure 4(a), we can see there are several frequency bands found below and above f_{ce} . The spectrogram is not similar to that of event 1. Note that the wave spectra presented in Figures 3 and 4 show broadband wave power, while this broadband power is not observed in Figure 2. Statistically, the type I and type III events usually show the narrow-band and broad-band power, respectively, while both narrow-band and broad-band wave power is observed in type II events. To identify which wave mode is involved in this event, we have presented the electric

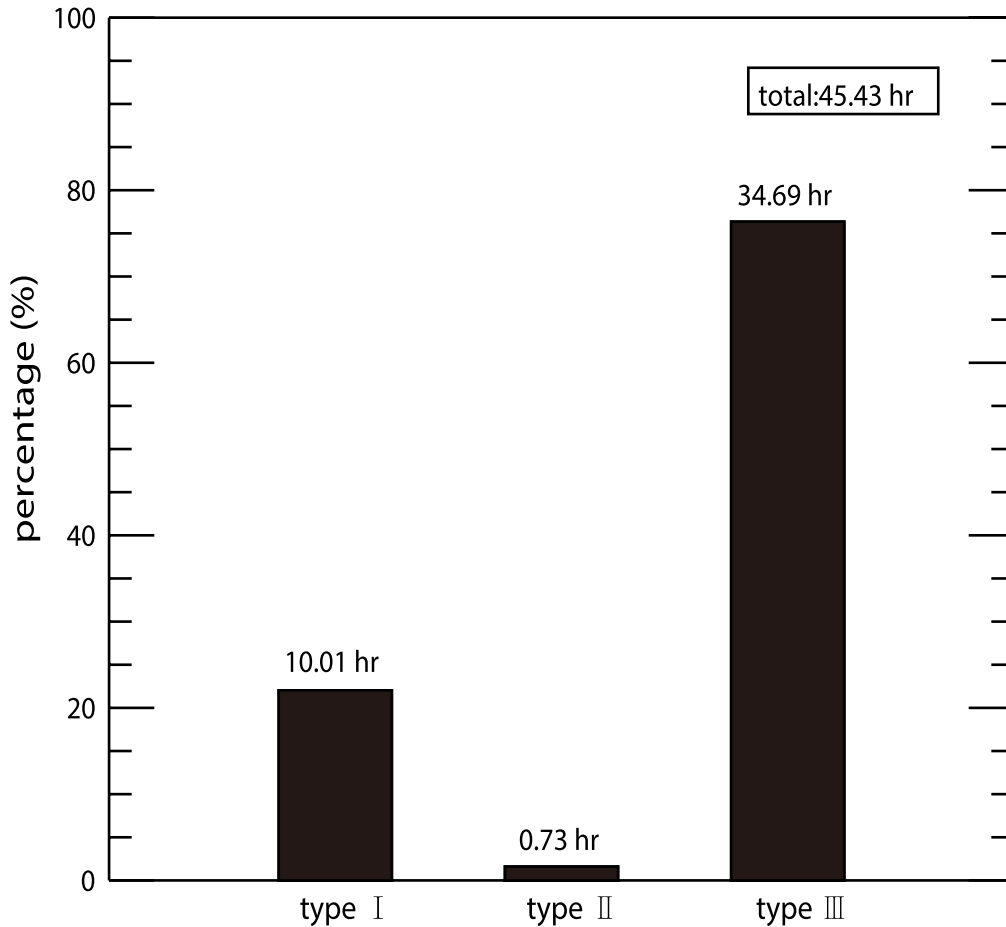


Figure 5. The percentage distribution of three types spectra near the f_{ce} .

power as a function of frequency at 01:04:28 UT. We note that the frequency band f_0 ($\sim 0.66f_{ce}$; solid magenta line) is considered to be the quasi-electrostatic whistler-mode wave and its second harmonic $2f_0$ (magenta dash line) can also be observed. Second, the frequency bands (f_{E1} and f_{E2} ; solid green lines) close to f_{ce} and $2f_{ce}$ are identified as an electron Bernstein wave. This is consistent with the type II spectrum. The most interesting feature is the frequency band marked by the blue line, whose frequency is just equal to the sum of the quasi-electrostatic whistler wave f_0 and first electron Bernstein wave f_{E1} . Its electric power is more than one order of magnitude smaller than either f_0 or f_{E1} . Figure 4(c) further displays the time profile of the peak wave power of valid wave signals for three bands, namely, f_0 , f_{E1} and $f_0 + f_{E1}$. The thicker solid line (band 1 and band 2) corresponds to the existence of band 3 (solid blue line). It is important to note that the frequency band $f_0 + f_{E1}$ can be observed only when both the f_0 and f_{E1} bands have sufficiently large wave power. These properties suggest that the $f_0 + f_{E1}$ band is excited due to the nonlinear coupling between the quasi-electrostatic whistler wave and the electron Bernstein wave. Such coupling has also been reported to occur in the Earth's magnetosphere (Gao et al. 2018b). Thus the type III wave event can be considered a mixture of whistler-mode and electron Bernstein waves and the nonlinear coupling between them.

4. Summary and Discussions

In this study, using PSP data, we have reported nonlinear wave-wave coupling related to whistler-mode and electron Bernstein waves in the near-Sun slow solar wind at a distance of ~ 36.6 to $\sim 38.2 R_S$ from the Sun. Based on the wave frequency and power, we found three types of electric spectra. The first is the quasi-electrostatic whistler-mode wave and its second harmonic, which resembles the quasi-electrostatic multiband chorus in the Earth's magnetosphere. The second is the pure electron Bernstein waves. The third is the mixture of whistler-mode and electron Bernstein waves. Note that the type III wave events are similar to the wave event reported in Malaspina et al. (2021). Malaspina et al. (2021) examined the burst data of near- f_{ce} waves during a time interval of ~ 3.5 s. In this study, we further find that nonlinear wave-wave coupling may also occur in type III wave events.

Using the power spectra data obtained from PSP during the first five solar encounters, we have selected all wave events with frequencies near f_{ce} . First, we select the wave events by requiring that the sum of the power spectral density in the frequency range ($0.3f_{ce} - 3f_{ce}$) at each point in time be greater than the threshold ($4 \times 10^{-10} \text{V}^2/\text{Hz}$). Then, this data point (0.87 s) is counted as one wave event. We also visually inspected these events and remove some anomalous events and noise. Finally, we classify the three types of wave events through spectral characteristics. We have analyzed all the data during the first five encounters and the total time is ~ 1460 hr. Figure 5 shows the percentage distribution of the three types of

spectra. In total, ~ 10 hr ($\sim 41,400$ time points) of data were found to include the type I spectrum (quasi-electrostatic whistler-mode wave and its second harmonic), ~ 0.73 hr (~ 3000 time points) of data including the type II spectrum (pure electron Bernstein waves), and ~ 34.7 hr ($\sim 143,500$ time points) of data including the type III spectrum (the mingling of whistler-mode and electron Bernstein waves). We find that the type III spectrum is most likely observed in the near-Sun solar wind. Based on previous theoretical studies (Ashour-Abdalla & Kennel 1978; Ashour-Abdalla et al. 1979; Neubert & Banks 1992; Menietti et al. 2002; Tripathi & Misra 2004), either the electron loss-cone distribution or an electron beam is unstable, which excites both the whistler-mode and electron Bernstein waves at the same time. To determine which electron distribution accounts for the wave spectrum near f_{ce} in the near-Sun solar wind requires in situ electron measurements with high time- and pitch angle- resolution. We will defer this for a future study.

Whistler-mode waves and electron Bernstein waves are widely detected in the Earth’s magnetosphere. Both wave modes play key roles in regulating electron dynamics. Moreover, satellite observations show that various nonlinear wave–wave coupling processes exist that are related to whistler-mode or electron Bernstein waves in the magnetosphere. The statistical results also revealed that whistler-mode chorus and its harmonics (also called “multiband chorus”) are very common phenomena. However, to our knowledge, such nonlinear wave–wave couplings have not been previously reported in interplanetary space. With the PSP data, we have found that the type I spectrum is quite similar to the quasi-electrostatic multiband chorus detected in the Earth’s magnetosphere. The fundamental wave (f_0) is below f_{ce} and the other wave occurs just lying on its second harmonic ($2f_0$). The power ratio between the fundamental wave and its second harmonic is between one and two orders of magnitude, which is also similar with observations in the Earth’s magnetosphere (Figures 3 and 8 in Gao et al. 2018a). In the type III spectra, we also find a relatively weaker wave mode that could be driven by the coupling between the whistler-mode (below f_{ce}) and electron Bernstein waves. This has also been observed in the Earth’s magnetosphere. Here we should mention that this wave mode may be too weak to be detected in some type III spectra.

We therefore propose that nonlinear wave–wave couplings in the solar wind may be as common as in the Earth’s magnetosphere, at least when one makes observations close to the Sun. Whistler-mode and electron Bernstein waves may play a crucial role in the evolution of the solar wind electron velocity distributions, and wave–particle interactions depend heavily on the spectral structure of plasma waves. Therefore, nonlinear wave–wave coupling related to whistler-mode or electron Bernstein waves may ultimately have some influence on the solar wind electron dynamics. The wave–wave coupling features noted in this paper taken at a distance of $\sim 37 R_S$ from the Sun have not been noted in the solar wind closer to the Earth. It can be expected that even stronger coupling may be found as PSP orbits closer to the source of the solar wind, i.e., the Sun.

This research was funded by the Strategic Priority Research Program of the Chinese Academy of Sciences Grant No. XDB41000000, the NSFC grant 41774151, 41631071, USTC Research Funds of the Double First-Class Initiative (YD3420002001), the Fundamental Research Funds for the Central Universities (WK3420000013), and “USTC Tang Scholar” program. We also acknowledge the entire Parker Solar Probe team, and the data used in this study can be downloaded from spdf.gsfc.nasa.gov.

ORCID iDs

Jiuqi Ma  <https://orcid.org/0000-0001-5665-3957>
 Xinliang Gao  <https://orcid.org/0000-0003-0767-2267>
 Zhongwei Yang  <https://orcid.org/0000-0002-1509-1529>
 Mingzhe Liu  <https://orcid.org/0000-0003-2981-0544>
 Quanming Lu  <https://orcid.org/0000-0003-3041-2682>

References

- Agapitov, O., Dudok de Wit, T., Mozer, F. S., et al. 2020, *ApJL*, 891, L20
 Ashour-Abdalla, M., & Kennel, C. 1978, *JGR*, 83, 1531
 Ashour-Abdalla, M., Kennel, C., & Livesey, W. 1979, *JGR*, 84, 6540
 Bale, S., Goetz, K., Harvey, P. R., et al. 2016, *SSRv*, 204, 49
 Burtis, W., & Helliwell, R. 1969, *JGR*, 74, 3002
 Case, A. W., Kasper, J., Stevens, M. L., et al. 2020, *ApJS*, 246, 43
 Cattell, C., Breneman, A., Dombeck, J., et al. 2021, *ApJL*, 911, L29
 Ellis, R., Jr., & Porkolab, M. 1968, *PhRvL*, 21, 529
 Fox, N. J., Velli, M. C., Bale, S. D., et al. 2016, *SSRv*, 204, 7
 Fredricks, R., & Scarf, F. 1973, *JGR*, 78, 310
 Gao, X., Lu, Q., Bortnik, J., et al. 2016, *GeoRL*, 43, 2343
 Gao, X., Lu, Q., & Wang, S. 2017, *GeoRL*, 44, 5269
 Gao, X., Lu, Q., & Wang, S. 2018a, *JGRA*, 123, 5506
 Gao, Z., Su, Z., Xiao, F., et al. 2018b, *GeoRL*, 45, 12685
 Harker, K., & Crawford, F. 1968, *JAP*, 39, 5959
 Helliwell, R. A. 1967, *JGR*, 72, 4773
 Home, R., Christiansen, P., Gough, M., et al. 1981, *Natur*, 294, 338
 Jagarlamudi, V. K., Alexandrova, O., Berčić, L., et al. 2020, *ApJ*, 897, 118
 Kajdič, P., Alexandrova, O., Maksimovic, M., Lacombe, C., & Fazakerley, A. 2016, *ApJ*, 833, 172
 Kasper, J. C., Abiad, R., Austin, G., et al. 2016, *SSRv*, 204, 131
 Kennel, C., Scarf, F., Fredricks, R., McGehee, J., & Coroniti, F. 1970, *JGR*, 75, 6136
 Lacombe, C., Alexandrova, O., Matteini, L., et al. 2014, *ApJ*, 796, 5
 Malaspina, D. M., Ergun, R. E., Bolton, M., et al. 2016, *JGRA*, 121, 5088
 Malaspina, D. M., Halekas, J., Berčić, L., et al. 2020, *ApJS*, 246, 21
 Malaspina, D. M., Wilson III, L., Ergun, R., et al. 2021, *A&A*, 650, A97
 Menietti, J., Santolík, O., Scudder, J., Pickett, J., & Gurnett, D. 2002, *JGRA*, 107, 1285
 Meredith, N. P., Horne, R. B., Thorne, R. M., & Anderson, R. R. 2009, *JGRA*, 114, A07218
 Moncuquet, M., Meyer-Vernet, N., Issautier, K., et al. 2020, *ApJS*, 246, 44
 Neubert, T., & Banks, P. M. 1992, *P&SS*, 40, 153
 Stansby, D., Horbury, T., Chen, C., & Matteini, L. 2016, *ApJL*, 829, L16
 Thorne, R. M. 2010, *GeoRL*, 37, L22107
 Tong, Y., Vasko, I. Y., Pulupa, M., et al. 2019, *ApJL*, 870, L6
 Tripathi, A., & Misra, K. 2004, *JASTP*, 66, 987
 Tsurutani, B. T., & Smith, E. J. 1974, *JGR*, 79, 118
 Vocks, C. 2012, *SSRv*, 172, 303
 Vocks, C., Salem, C., Lin, R., & Mann, G. 2005, *ApJ*, 627, 540
 Whittlesey, P. L., Larson, D. E., Kasper, J. C., et al. 2020, *ApJS*, 246, 74
 Wilson, L., III, Cattell, C. A., Kellogg, P. J., et al. 2010, *JGRA*, 115, A12104
 Zhang, Y., Matsumoto, H., & Kojima, H. 1998, *JGR*, 103, 20529